# Van der Waals Epitaxy of Pulsed Laser Deposited Antimony Thin Films on Lattice-matched and Amorphous Substrates

Yimam, Daniel; Ahmadi, Majid; Kooi, Bart

*Published in:*
Materials today nano

*DOI:*
10.1016/j.mtnano.2023.100365



*Publication date:*
2023

Materials Today Nano 23 (2023) 100365

Contents lists available at ScienceDirect

Materials Today Nano

journal homepage: https://www.evise.com/profile/#/MTNANO/login

# Van der Waals epitaxy of pulsed laser deposited antimony thin films on lattice-matched and amorphous substrates

D.T. Yimam*, M. Ahmadi, B.J. Kooi**

*Zernike Institute for Advanced Materials, University of Groningen, Nijenborgh 4, Groningen 9747 AG, the Netherlands*

ARTICLE INFO

*Article history:*
Received 15 March 2023
Received in revised form
2 June 2023
Accepted 11 June 2023
Available online 15 June 2023

*Keywords:*
Van der Waals epitaxy
Monatomic antimony thin films
Antimonene
Phase change materials
Pulsed laser deposition
2D materials

ABSTRACT

Monatomic antimony thin films have recently attracted attention for applications in phase change memory, nanophotonics, and two-dimensional materials. Although some promising results have been reported, the true potential of Sb thin films is still hindered by the scalability issue and the lack of reliable bottom-up production. Here we demonstrate the growth of Sb thin films on a lattice-matching and amorphous substrates using pulsed laser deposition. C-axis out-of-plane textured Sb thin films were successfully deposited on $Sb_2Te_3$ and $SiO_2/Si_3N_4$ substrates. In the case of growth on $Sb_2Te_3$, we show that an intermediate phase is formed at the $Sb_2Te_3$–Sb interface playing a crucial role in forming a solid coupling and thus maintaining epitaxy leading to the production of high-quality Sb thin films. A 3–4 nm amorphous Sb seed layer was used to induce texture and suitable surface termination for the growth of Sb thin films on amorphous substrates. The deposition parameters were fine-tuned, and the growth was monitored *in situ* by reflection high energy electron diffraction. Scanning/transmission electron microscopy unveiled the local structure of produced films showing the formation of β-phase Sb thin films. Our results demonstrate the feasibility to produce very smooth high-quality antimony thin films with uniform coverage, from few layers to large thicknesses, using pulsed laser deposition. We believe the results of our work on scalable and controllable Sb growth have the potential to open up research on phase change materials and optoelectronics research.


## 1. Introduction

The success of graphene opened a gate of new research to find two-dimensional (2D) materials with attractive properties [1]. There is great interest, due to excellent properties such as topological insulator and tunable band gap, in elemental 2D materials, including layered antimony (Sb) [2,3]. The added structural stability in an ambient atmosphere, as opposed to black phosphorus [4], and the theoretically predicted large bandgap [5] gave Sb an edge against other elemental layered materials for future optoelectronic applications. The surface termination of substrates and passivated layers play a crucial role during the growth of highly textured crystals [6–8]. Surface passivation was previously used to reconstruct the Si dangling bonds by elements like Sb and Bi so that improved epitaxy can be achieved [7,9,10]. Although the passivation resolved the strain buildup from the lattice mismatch of most chalcogenides with Si [11], the process required additional steps to remove the native oxide and reconstruct the Si surface by annealing at a high temperature. Recently, it has become a common practice to directly grow epitaxial films on an amorphous substrate with a two-step method using a seed layer [12,13]. Strictly speaking, achieving epitaxial growth on amorphous substrates like SiO2 is impossible and a crystalline substrate is needed for van der Waals (vdW) epitaxial growth. However, with a two-step growth method, the seed layer produces a suitable surface termination for subsequent growth by vdW epitaxy and particularly quintuple-based materials like $Sb_2Te_3$, $Bi_2Te_3$, and $Bi_2Se_3$, also well-known as topological insulators, turned out effective as seed layers to grow films by homoepitaxy [13] and heteroepitaxy [14–16]. These quintuple-based materials are also suitable substrates for depositing a few layers of antimony thin films. Previous works on the 2D—2D growth of Sb on lattice matching Te and Se—terminated topological insulators have shown the possibility of producing high-quality films with attractive topological surface states [17–22].

Another avenue where elemental antimony thin films have attracted interest is for their phase-switching properties. It has

* Corresponding author.
** Corresponding author.
*E-mail addresses:* d.t.yimam@rug.nl (D.T. Yimam), b.j.kooi@rug.nl (B.J. Kooi).

https://doi.org/10.1016/j.mtnano.2023.100365

been shown that the rapid crystallization of bulk Sb is avoided by confining amorphous Sb in films of only a few nm thick [23,24]. The confinement of Sb thin films increased the amorphous phase stability by retarding the structural relaxation over time [25]. Soon after stabilizing the amorphous phase, many findings emerged with applications utilizing the optical and electrical contrasts between the amorphous and crystalline phases of monatomic Sb thin films. From nanophononics and optoelectronics [26–28] to phase change memory [23,29] and neuromorphic architectures [24], monatomic Sb shows great promise for future applications. The functionality is extended further with an added degree of freedom because the properties of Sb thin films depend strongly on thickness in this few nm thick range [26,28]. Although complex phase change material alloys, for example $Ge_2Sb_2Te_5$, were considered to have best properties, the 'elemental' nature of monatomic Sb comes with an upper hand from the thin film production side and phase change memory device endurance perspective. Some ternary and quaternary phase change materials (in particular Ge- and Te-rich GST for example) suffer from compositional variations and phase separation during successive phase switching [30,31]. Indeed, monatomic antimony thin films will not have these problems.

Proper growth control of high-quality antimony films is of great importance, given the current interest in the material's properties for potential applications in different fields of study. Hence, here we report the vdW epitaxy growth of monatomic Sb thin films on a lattice-matched substrate $Sb_2Te_3$ and on an amorphous surface ($SiO_2$) using pulsed laser deposition (PLD). So far, the majority of reported results on the growth of layered Sb employed molecular beam epitaxy (MBE) [21,32–36], and a small number of results used other techniques like exfoliation [4,37] and physical and chemical vapor deposition [38–41]. MBE is very powerful and versatile in the growth of high-quality crystals. However, the lattice-matching requirement and the need for surface reconstruction hinder the technique's applicability to a broader selection of materials and substrates [42]. Moreover, smooth Sb films showing uniform coverage over large area have not been produced using MBE [21,32–36].

PLD provides a practical alternative with exact stoichiometry transfer, fast and flexible growth conditions, and a relatively low substrate temperature needed to produce high-quality layered crystals [43]. So far, to our knowledge, no reported result exists for the vdW epitaxy growth of monatomic Sb thin films by PLD. In addition to the vdW epitaxy of antimony on a lattice-matching $Sb_2Te_3$ seed layer, we show the possibility of producing high-quality layered Sb crystals on an amorphous substrate in a two-step growth method. The quality of Sb thin films was monitored *in situ* by a reflection high-energy electron diffraction (RHEED) setup. The production of high-quality films is confirmed by atomic-resolution imaging using scanning transmission electron microscopy (STEM). In addition, the full coverage and smoothness of the produced films were characterized using scanning electron microscopy (SEM) and atomic force microscopy (AFM). Our work shows substantially improved quality antimony films and thereby opens up several avenues from the production and application perspective in the fields of phase change memory, nanophononics, and optoelectronics.

## 2. Experimental methods

**Sample preparation and thin film growth:** For $Sb_2Te_3$–Sb heterostructure depositions, a seed layer of 200 pulses (3–4 nm thick) of $Sb_2Te_3$ was deposited at room temperature. After the deposition, the sample was annealed to 210 °C to crystallize and to enable epitaxy with c-axis out-of-plane. The deposition of $Sb_2Te_3$ is then continued at 210 °C. After the $Sb_2Te_3$ deposition, the process is continued with Sb deposition. All depositions were done with a PLD system using KrF excimer laser (wavelength of 248 nm). The deposition parameters were optimized beforehand by varying them during extensive tests across parameter space. A laser fluence of 0.8 J/cm$^2$, a repetition rate of 1 Hz, and a processing gas (Argon) pressure of 0.12 mBar were used for $Sb_2Te_3$ depositions. Furthermore, a laser fluence of 1.5 J/cm$^2$, a repetition rate of 3 Hz, and a processing gas pressure of $10^{-3}$ mBar were used for Sb depositions. After every deposition, the samples were capped by a 5–10 nm thick $LaAlO_x$ (with x close to 3) layer to prevent surface oxidation and chemical contamination. Before every deposition, the $Si/SiO_2$ substrates were chemically cleaned. The cleaning steps include sonication in isopropanol for 20 min and flushing with ethanol. The film growth and epitaxy were monitored by an *in situ* reflection high-energy electron diffraction (RHEED) setup with an accelerating voltage of 30 kV. The grazing incident (2–3° normal to the substrate) electron beam provides information on the top few atomic layers of the deposited film. RHEED images were collected every 300 ms during depositions.

**Morphological characterization using SEM and AFM**: For morphological and structural characterizations, a set of samples were prepared on $Si/SiO_2$ substrates and $Si_3N_4$ TEM membranes. SEM (FEI NovaNanoSEM 650 and FEI Helios G4 CX) was used to characterize the surface morphology of the deposited thin films. In addition, AFM images were collected by a Bruker Multimode 8 instrument, and the images were analyzed by the Gwyddion software.

**Focused ion beam sample preparation:** The FEI Helios G4 CX dual-beam SEM–focused ion beam was used to prepare an e-transparent sample. First, the protective EBID (electron beam induced deposition) carbon(C) and platinum (Pt) were deposited on the film before IBID (ion beam induced deposition) Pt protective layer. Next, cross-sectional chunks (dimensions: 15 × 2.0 × 5 μm$^3$) were made and transferred using easylift™ needle to the copper half-grid. Then the sample was thinned down to 80–100 nm thickness using standard Ga-beam processing at 30 kV with an opening window (6.0 × 5.0 μm$^2$). The remaining chunk is left thick to have a rigid frame to minimize the bending and stress released in the e-transparent window. Finally, several low kV cleaning steps (5 and 2 kV) were used to clean the side surfaces of the lamella.

**High-resolution STEM imaging:** The focused ion beam prepared sample and loaded to the TEM grid was transferred to the TEM using a dedicated double tilt TEM holder optimized to collect X-rays in the TEM. The microstructure imaging of plan-view and cross-sectional layered antimony films were examined with a double-corrected and monochromated Themis Z STEM (Thermo Fisher Scientific) operating at 300 kV and equipped through high-angle annular dark-field (HAADF) STEM and integrated differential phase contrast STEM using ~80% coverage of a 4-segmented DF detector. The beam convergence angle was measured at ~24.0 and ~35 mrad mrad (for the thin sample with small grains) and the probe current of 20 pA was used for STEM imaging. Energy-dispersive X-ray (EDX) spectroscopy results were achieved with a Dual X EDX system (Bruker) using two large area detectors, capturing 1.76 steradians with a probe current of 100 pA. Data acquisition and analysis were done using Velox software.

## 3. Results and discussion

*In situ* RHEED measurements can provide relevant information about thin film morphology, quality, and crystallinity during depositions [14–16]. Fig. 1 shows RHEED images captured during Sb thin film depositions on $Sb_2Te_3$ and Sb seed layers. The figures provide information about individual interfaces in the heterostructures, starting from the initial $SiO_2$ substrate to the final Sb

layers. Fig. 1a presents a cloudy RHEED pattern of the starting thermal oxide substrate. The deposition starts with a 3–4 nm thick $Sb_2Te_3$ seed layer at room temperature. This first layer is amorphous, as confirmed by RHEED in Fig. 1b, since the deposition is at room temperature. The idea here is to control the out-of-plane epitaxy by the self-organizing nature of the seed layer upon heat treatment [12]. Once the seed layer is annealed to the deposition temperature, 210 °C in our case, the 3–4 nm thick seed layer crystallizes in a fashion with self-alignment of specific crystallographic planes parallel to the surface. Here, the initial amorphous $Sb_2Te_3$ layer crystallizes with the c-axis out-of-plane because the quintuples blocks with vdW like bonding between them align parallel to the surface. Fig. 1c shows the RHEED pattern of the seed layer after annealing to 210 °C. A sharp, streaky pattern indicates a smooth surface and high crystallinity. Note that although the seed layer induced a purely c-axis out-of-plane epitaxy, the in-plane orientation of the crystalline grains is random. Soon after the $Sb_2Te_3$ seed layer's crystallinity and epitaxy are confirmed, Sb growth is started at 210 °C. Fig. 1d shows the RHEED pattern after 20 nm Sb layer deposition. The streaky patterns progressed throughout the Sb thin film thickness, indicating that in addition to the surface smoothness, the c-axis out-of-plane epitaxy is maintained.

$Sb_2Te_3$ is carefully selected as a seed layer for Sb growth for several crucial reasons. The first reason is the similarity of the crystal structures of both $Sb_2Te_3$ and Sb layers. The $Sb_2Te_3$ quintuple layers crystallize in a trigonal crystal structure (space group R $\bar{3}$ $m$) where the two cation Sb atoms and the three anion Te layers are stacked along the c-axis [33,44,45]. Monatomic antimony has the same trigonal crystal structure, where bilayers of Sb are stacked along the c-axis out-of-plane orientation (see the cross-section images below in Fig. 3). Moreover, the Te termination of the last quintuple layer in $Sb_2Te_3$ is ideal for the vdW epitaxy of Sb bilayers for a layer-by-layer growth mode. Another reason is the nearly perfect lattice match of the $Sb_2Te_3$ quintuple layers with the Sb bilayers. The structure of $Sb_2Te_3$ (a = 4.264 Å and c = 30.458 Å) and Sb (a = 4.30 Å and c = 11.22 Å) have an in-plane lattice mismatch of <1%, which can be considered as a perfect lattice match since the slight mismatch can easily be accommodated (gradually) at the vdW-like gaps in the Sb top layer similar to the strain relaxation behaviors observed between all pairwise combinations of $Sb_2Te_3$, $Bi_2Te_3$, and GeTe [14,15].

The heteroepitaxy growth of Sb on the $Sb_2Te_3$ seed layer produced smooth and high-quality films. Therefore, the same process can be applied using directly Sb as seed layer for the subsequent Sb growth. After optimization of the PLD conditions, we also in this case grow crystalline Sb thin films in which all domains have their c-axis out-of-plane, i.e. with the Sb bilayers parallel to the $SiO_2$ surface. The RHEED pattern images collected during the homoepitaxy growth of Sb thin films on the Sb seed layer are presented in Fig. 1e–f. Here, similar to when the $Sb_2Te_3$ seed layer was used, the complete interface information is presented in sequence starting from the $SiO_2$ substrate in Fig. 1e. In Fig. 1f and g, the Sb seed layer deposition at room temperature and after annealing to the

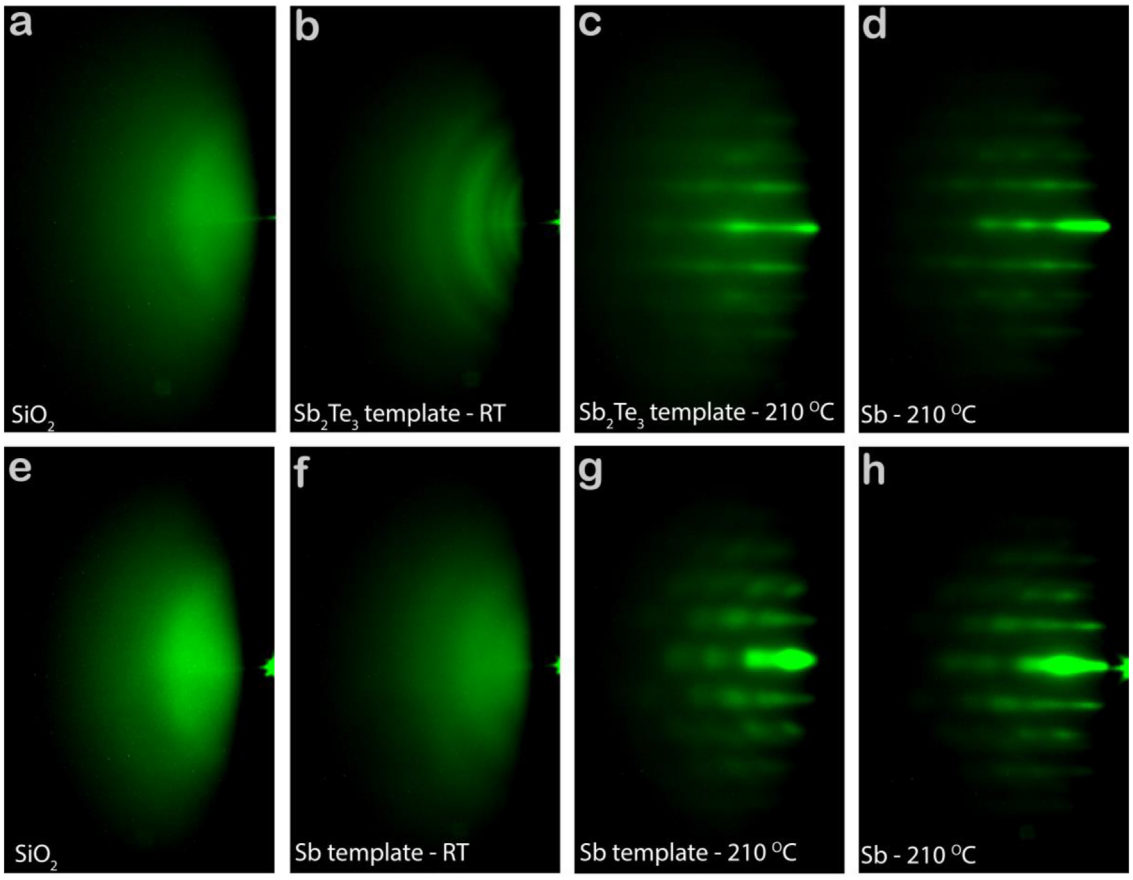


**Fig. 1.** RHEED pattern images of Sb deposition on Te- and Sb-terminated seed layers of $Sb_2Te_3$ and Sb. In (a) and (e), the RHEED patterns of the starting thermally grown $SiO_2$ substrates are shown. The $SiO_2$ layers have a thickness of 300 nm. A few layers (3–4 nm thick) of (b) $Sb_2Te_3$ and (f) Sb seed layers were deposited on the $SiO_2$ substrate. Seed layers of $Sb_2Te_3$ (c) and Sb (g) were annealed to 210 °C to induce the c-axis out-of-plane texture. After annealing the seed layers, Sb growth continued. The RHEED patterns in (d) and (h) show the final film texture after Sb's heteroepitaxial and homoepitaxial growth consecutively.

deposition temperature of 210 °C are shown, respectively. As expected, the room temperature deposited 3–4 nm Sb layer is amorphous (confirmed by the cloudy RHEED image), and the annealed layer is crystalline with a streaky RHEED pattern showing the c-axis out-of-plane epitaxy formation. Furthermore, as confirmed by RHEED in Fig. 1h, the c-axis out-of-plane epitaxy is maintained when growth continues at 210 °C. The homoepitaxy growth of Sb on the Sb seed layers is preferred compared to the heteroepitaxy growth of Sb on the $Sb_2Te_3$ seed layer. In addition to the 'chemical consistency,' the lack of strain from the exact lattice template is a large advantage.

Fig. 2 shows the morphology and plan-view structural analysis of Sb films on the $Sb_2Te_3$ seed layer, where the heterostructure schematics are illustrated in Fig. 2a. During deposition, thermal oxide and $Si_3N_4$ membrane were used to couple the large area SEM and AFM characterizations to a local STEM characterization. Fig. 2b and c show the images from the surface morphology characterizations using SEM and AFM, respectively. The observed morphologies provide crucial information about film quality, grain size, and surface roughness. Crystal domains of ≈200 nm in size are stacked together laterally. From the AFM scan in Fig. 2c, the root-mean-square roughness of a 20 nm Sb film on a 12 nm $Sb_2Te_3$ layer is determined to be 0.9 nm indicating a smooth surface. Although PLD-grown amorphous films generally have a very smooth surface, this is not the case for crystalline films. When transferring ablated plasma plume to a substrate, multiple parameters determine the type of growth for the formed crystal. From laser energy and repetition rate to substrate temperature and processing gas pressure, parameter optimization is necessary to access the desired growth type. To achieve smooth crystalline Sb films with large grain sizes and uniform coverage, combining a low Ar background pressure with an increased laser repetition rate (from 1 Hz to 3 Hz in this case) is required. The combined PLD optimization thus produced for a heterostructure of 12 nm $Sb_2Te_3$ and 20 nm Sb thin film a uniform surface coverage over cm sized area with low root-mean-square roughness of ≈0.9 nm and with grains that have their c-axis out-of-plane and have sizes of ≈200 nm. Supplementary Information Fig. S1 provides a detailed explanation of parameter optimization toward this layer-by-layer growth.

For high-resolution HAADF-STEM imaging of Sb thin films grown on a $Sb_2Te_3$ seed layer, deposition has been done on a $Si_3N_4$ membrane. Here the $Sb_2Te_3$ layer thickness has been set to 3–4 nm to minimize the seed layer effect for the plan-view imaging. Fig. 2d presents a large area HAADF-STEM image showing multiple grains covering the $Si_3N_4$ substrate surface. The average grain size here is ≈ 80–90 nm. The reduced crystal grain size is associated with the thinner $Sb_2Te_3$ seed layer, *i.e.* the lateral domain size increases when the $Sb_2Te_3$ film growth is continued at 210 °C. As a result, larger crystals have been deposited with a thicker $Sb_2Te_3$ bottom layer of 12 nm in thickness observable in the cross-section image of a sample with about 20 nm Sb film on top (see Fig. 3a). A high-resolution atomic image of a specific Sb crystal is provided in Fig. 2e, with an enlarged image given in Fig. 2f. A clear hexagonal periodicity corresponds to the [0001] zone axis of β-phase antimony.

A cross-section atomic-resolution HAADF-STEM image of the $Sb_2Te_3$–Sb heterostructure is shown in Fig. 3a, with the enlarged part in Fig. 3b. The cross-section image in Fig. 3a shows sharp interfaces between the $SiO_2$ substrate, the stacked quintuple $Sb_2Te_3$ layers, and the Sb bilayers. In HAADF-STEM mode, the atomic columns are always the bright spots in a dark surrounding, and the brightness of the spots scales with the average atomic number Z of

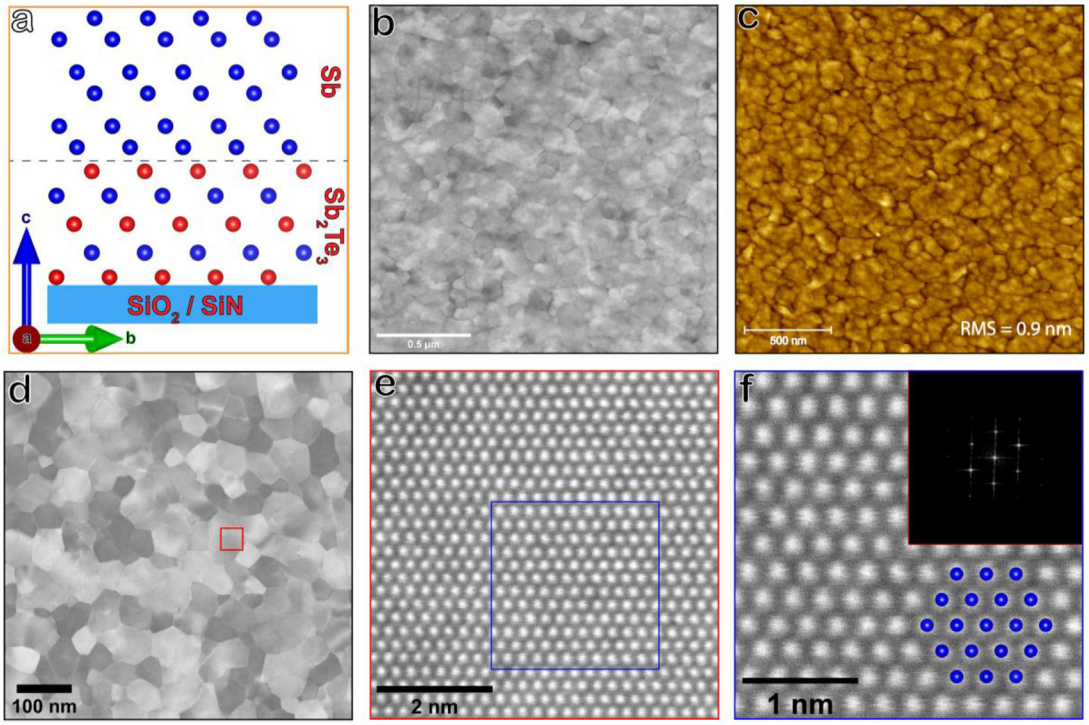


**Fig. 2.** Large and small area plan-view characterization of Sb grown on $Sb_2Te_3$ seed layer. (a) A schematic diagram shows Sb's c-axis out-of-plane growth on the $Sb_2Te_3$ seed layer on amorphous substrates. (b) An SEM and (c) AFM scan images of 20 nm Sb thin film grown at 210 °C on a 12 nm $Sb_2Te_3$ layer. Crystal grains with lateral sizes of ≈200 nm have a sharp c-axis out-of-plane texture but with a random in-plane orientation. The root-mean-square (RMS) roughness of 0.9 nm indicates a smooth surface. (d) A large area HAADF-STEM image of Sb grown on 3–4 nm $Sb_2Te_3$ seed layer. Crystal grains of ≈90 nm stacked laterally, covering the entire $Si_3N_4$ substrate surface. (e) High-resolution HAADF-STEM image of one of the crystal grains seen in (d), and (f) an enlarged image of the Sb atoms with a schematic showing overlaying the hexagonal Sb lattice and the FFT in the inset. AFM, atomic force microscopy; FFT, fast Fourier transform; HAADF-STEM, high-angle annular dark-field scanning transmission electron microscopy; SEM, scanning electron microscopy.

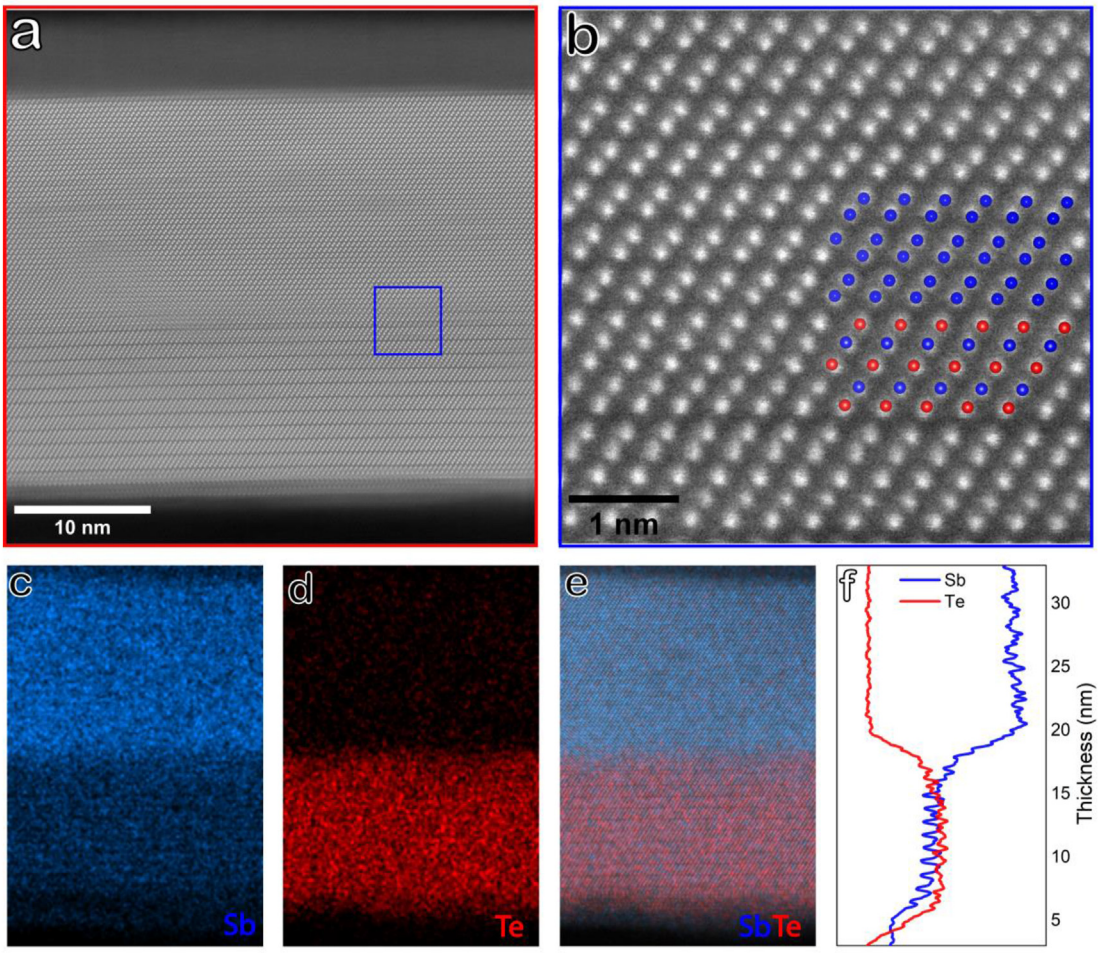


**Fig. 3.** Cross-section STEM results for an Sb film ( ≈20 nm thick) on a ≈12 nm thick $Sb_2Te_3$ layer. The deposition started with a 3–4 nm $Sb_2Te_3$ seed layer on a silicon wafer covered with thermal oxide. The growth direction in all images is from bottom to top. (a) STEM–HAADF images show a complete overview of the whole layer containing the $Sb_2Te_3$ bottom layer and the Sb top layer. (b) Enlarged part of (a) showing the atomic structure and epitaxy of Sb on $Sb_2Te_3$ more clearly. In (c) and (d), STEM–EDX color map (based on spectrum imaging, i.e. for each pixel an EDX spectrum is recorded) showing the distribution of Sb in blue and Te in red. (e) A combined (Sb and Te) elemental mapping with clear color contrast near the $Sb_2Te_3$–Sb interface, and in (f), STEM–EDX line profiles for Sb (blue line) and Te (red line). EDX, energy-dispersive X-ray spectroscopy; HAADF, high-angle annular dark-field; STEM, scanning transmission electron microscopy.

the columns. Due to the closeness of Sb and Te atoms in the periodic table, their Z contrast is (unfortunately) negligible. Still, the $Sb_2Te_3$ quintuples (Te–Sb–Te–Sb–Te units) and the Sb bilayers can be distinguished readily in Fig. 2a and b. Indeed, the layers are aligned parallel to the substrate surface, and the Sb grows epitaxially on the Sb2Te3. STEM–EDX elemental mapping of the Sb–$Sb_2Te_3$ heterostructure is presented in Fig. 2c–f. From the elemental mapping results, the Sb and $Sb_2Te_3$ layers are identifiable, and it can be assured that there is a uniform Sb layer on top of the $Sb_2Te_3$ layer.

The HAADF-STEM images of the $Sb_2Te_3$–Sb cross-section show the lattice-matched epitaxy, where the $Sb_2Te_3$ layer is a suitable template for Sb growth. However, a more intricate interesting effect can be observed at the interface, where the last $Sb_2Te_3$ quintuple layer and the first Sb bilayer couple (to form a new phase), see Fig. 4. The last distinctly observable $Sb_2Te_3$ quintuple occurs at the lower blue box, and the first clearly observable Sb bilayer occurs at the upper blue box in Fig. 4a and in the magnified image of the interface in Fig. 4b. In-between, inside the overlayed red box, there is a vdW block of seven atomic layers which can be typified as a $Sb_4Te_3$ layer (i.e. Te–Sb–Te–Sb–Te–Sb–Sb units) [46–48]. So, the actual position of the interfaces is indicated by the interfaces of the red and blue overlayed boxes. However, the interface is not formed by a similar width vdW-like bonding, such as between the $Sb_2Te_3$ quintuples or between the Sb bilayers, but by a shorter and thus stronger (more covalent/metavalent) bond. These distances can be readily quantified based on direct measurements in the line scans presented at the left side of Fig. 4a and the right side of Fig. 4b. The vdW-like gaps between the $Sb_2Te_3$ have a size of 278 ± 4 p.m. Similarly, the vdW-like gap between the Sb bilayer is 244 ± 4 p.m. However, at the interface between $Sb_2Te_3$ and Sb, *i.e.* within the $Sb_4Te_3$ layer, the gap between the last Te-plane and the first Sb plane on top is 219 ± 4 p.m. So, this is even 10% smaller than the vdW-like gap between the bilayers in Sb.

Another piece of evidence for the presence of a new phase at the $Sb_2Te_3$–Sb interface comes from the high-resolution image analysis of Fig. 4a using the software tool Atomap [49]. Here, the interplanar distance differences in vertical direction (parallel to c-axes of $Sb_2Te_3$ and Sb) are extracted and plotted in Fig. 4c after the position of each atomic column is accurately determined and horizontal atomic planes are constructed. The color contrast gives the interplanar distance differences, yellow being the largest and blue the smallest. As indicated by the red arrows, the vdW-like gaps are readily visible with the highest distance difference as they should be. The distance difference also holds for the gaps in the bilayers of

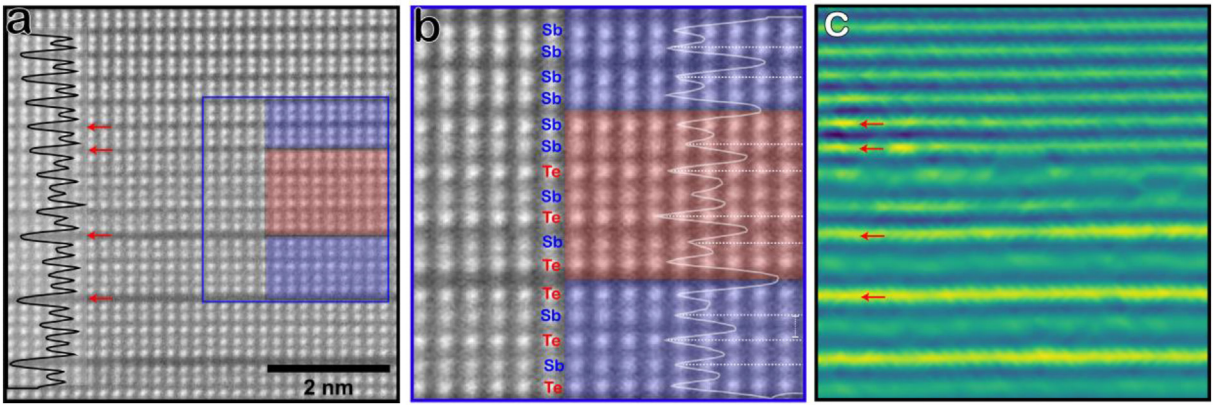


**Fig. 4.** A new phase of $Sb_4Te_3$ is formed at the $Sb_2Te_3$–Sb interface. (a) Atomic-resolution HAADF-STEM image of the Sb–$Sb_2Te_3$ interface with the line profile overlayed on the left. Lower blue box on the right shows the $Sb_2Te_3$ layer on the bottom, upper blue box the Sb bilayers on the top, and the red box the intermediate new layer of seven atomic planes of $Sb_4Te_3$. (b) An enlarged image of (a), with the line profile on the right. (c) The color map of the monolayer distance difference from the Atomap software tool. The large distance differences, i.e. the vdW-like gaps, are bright yellow. At the interface between the last $Sb_2Te_3$ and the first Sb, within the $Sb_4Te_3$, the vdW-like gap disappears. HAADF, high-angle annular dark-field; STEM, scanning transmission electron microscopy.

Sb atoms, alternating long and short distances between atomic layers. When looking closer to the interface, the last $Sb_2Te_3$, and the first Sb, we notice that the color contrast vanishes, indicating a reduced distance difference. Therefore, strong evidence is provided that a new phase, $Sb_4Te_3$, is formed at the interface with relatively strong coupling between the last $Sb_2Te_3$ and the first Sb bilayer on top, such that an excellent epitaxy of Sb on $Sb_2Te_3$ is achieved.

The more important novelty of this work, in addition to the layer-by-layer growth of Sb on a lattice-matched $Sb_2Te_3$ template layer, is the homoepitaxy growth of Sb. Instead of Sb2Te3, Sb can also be used as a seed layer, and then pure and highly textured Sb films can be grown. Again, films uniformly covering the substrate can be produced where all domains have their c-axis out-of-plane. Similar to the $Sb_2Te_3$ seed layer, the deposition starts with a 3–4 nm amorphous Sb thin film deposited on the $SiO_2$/Si and $Si_3N_4$ substrates at room temperature. In our previous work, we showed how accurately we could produce smooth amorphous Sb thin films with thicknesses ranging between 2.7 and 6.0 nm with complete surface coverage over large areas [28]. Once the sample is annealed to the deposition temperature of 210 °C, the amorphous Sb layer crystallizes in the trigonal crystal structure (the same space group as $Sb_2Te_3$) with c-axis out-of-plane orientation where Sb bilayers are stacked together with a vdW-like gap between them. After the c-axis epitaxy is induced in the seed layer, Sb deposition is continued at 210 °C. The layer-by-layer growth will then follow the initial Sb seed layer lattice. The RHEED pattern images in Fig. 1e–h show the deposition process of Sb on the Sb seed layer. After deposition, the morphology and structure of the Sb thin films were investigated using HAADF-STEM. A plan-view image of Sb thin film prepared on a $Si_3N_4$ substrate is shown in Fig. 5, with the homoepitaxy ' heterostructure' schematically depicted in Fig. 5b.

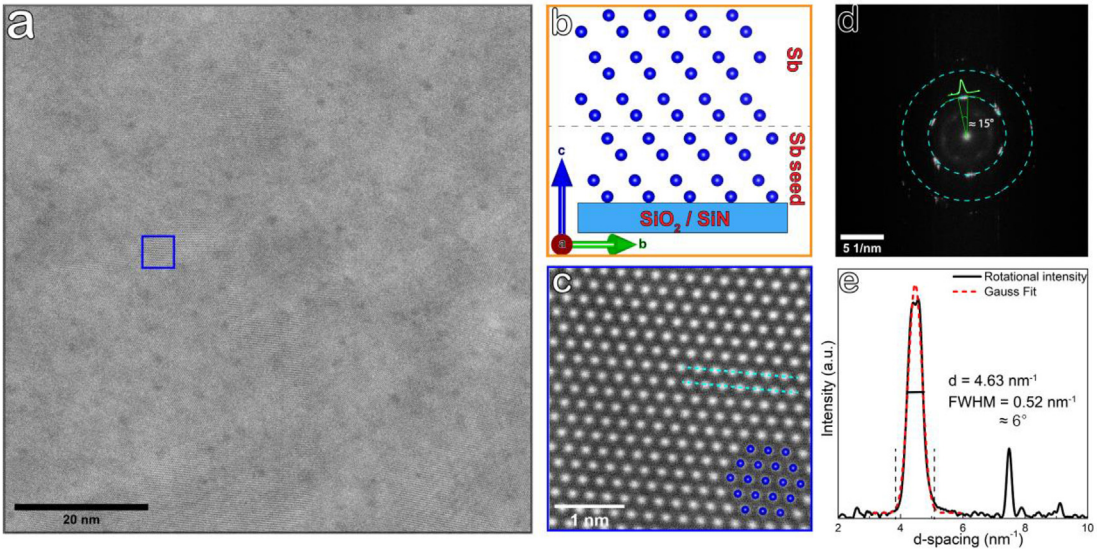


**Fig. 5.** High-resolution plan-view imaging of Sb thin films produced using an Sb seed layer. A large area view of the film surface, with multiple Sb crystal grains, is shown in (a). No opening between grains and the FFT in (d) confirms the c-axis out-of-plane texture. The FFT spots in (d) have an angular spread of ≈15° between all crystal grains. The schematic for the homoepitaxy growth of Sb is presented in (b). Here, the first 3–4 nm thick Sb layer was first used as a seed layer to promote texture. Atomic-resolution imaging of a single Sb crystal is shown in (c). The overlaying hexagonal Sb lattice confirms the production of β-phase Sb thin films. In (e), the average rotational intensity of the FFT pattern shown in (d) is presented. The central peak corresponds to a d-spacing of 4.63 $nm^1$, and from the central peak's Gauss fit, the FFT spots spread is expressed with a FWHM value of 0.52 $nm^1$ corresponding to ≈6° spread. FFT, fast Fourier transform; FWHM, full width at half maximum.

A homogeneous coverage of Sb thin films with c-axis out-of-plane orientation is seen in Fig. 5a and the inset fast Fourier transform (FFT) pattern. Here, similar to Sb thin films deposited on the $Sb_2Te_3$ seed layer, the in-plane randomly oriented crystal grains are stacked together laterally without openings, creating a smooth surface (see Supplementary Information Fig. S3). However, the lateral sizes of the domains are substantially smaller in this case, only 15–20 nm, and thus remain similar to the film thickness. It is worth mentioning here that the linear correlation between laser pulse number with thickness means we can also produce Sb films ranging from a few bilayers to larger thicknesses.

From the FFT pattern in Fig. 5d, all grains within the field of view of Fig. 5a are highly c-axis out-of-plane oriented, and the in-plane orientation is limited to a slight angle rotation ($\approx 15^\circ$ for all). The limited a–b-axis rotation is evident in the FFT pattern where we would have expected circular rings as seen in the Supplementary Information Fig. S4 for random in-plane orientation, but here, the spots do not makeup rings. In turn, diffraction spots from individual grains are close to each other with a slight orientation change. Therefore, we can extract the approximate spread angle for most crystal grains from the average rotational intensity and the full width at half maximum of the intensity peak. As illustrated in Fig. 5e, the start and end of the central intensity peak, $\approx 3.83$ $nm^{-1}$ and $\approx 5.14$ $nm^{-1}$, with a difference of $\approx 1.31$ $nm^{-1}$, correlates to the $\approx 15^\circ$ measured in Fig. 5d. From the Gauss fit of the intensity peak in Fig. 5e, the full width at half maximum value of $\approx 0.52$ $nm^{-1}$ is extracted, which correlate with an average rotation angle of $\approx 6^\circ$. Note that this is indeed dependent on the analyzed area where the in-plane orientation change is limited for small areas (for example, for an area in Fig. 5a), and the orientation is completely random for large areas (as seen in the Supplementary Information Fig. S4). Finally, high-resolution atomic imaging of a single crystal grain is presented in Fig. 5c. Similar to what we imaged for Sb grown on $Sb_2Te_3$, the hexagonal periodicity is seen, confirming the growth of trigonal β-phase antimony.

As previously mentioned, the Sb growth on amorphous substrates starts with a few layers of Sb (antimonene) with a preferred c-axis out-of-plane orientation. Fig. 6a shows a cross-sectional BF-TEM image of the few layers of antimonene grown on $SiO_2$ substrate. The layer has a thickness of only 3–4 nm. Starting from an amorphous phase and subsequently crystallizing, the thin layer induced a crystalline phase with a preferred of c-axis out-of-plane orientation. This orientation is visible in Fig. 6b where an integrated differential phase contrast-STEM image shows the Sb bilayers stacked together when viewed in [11 $\bar{2}$ 0] zone axis. More details about the few layers of antimonene production and characterization are provided in the

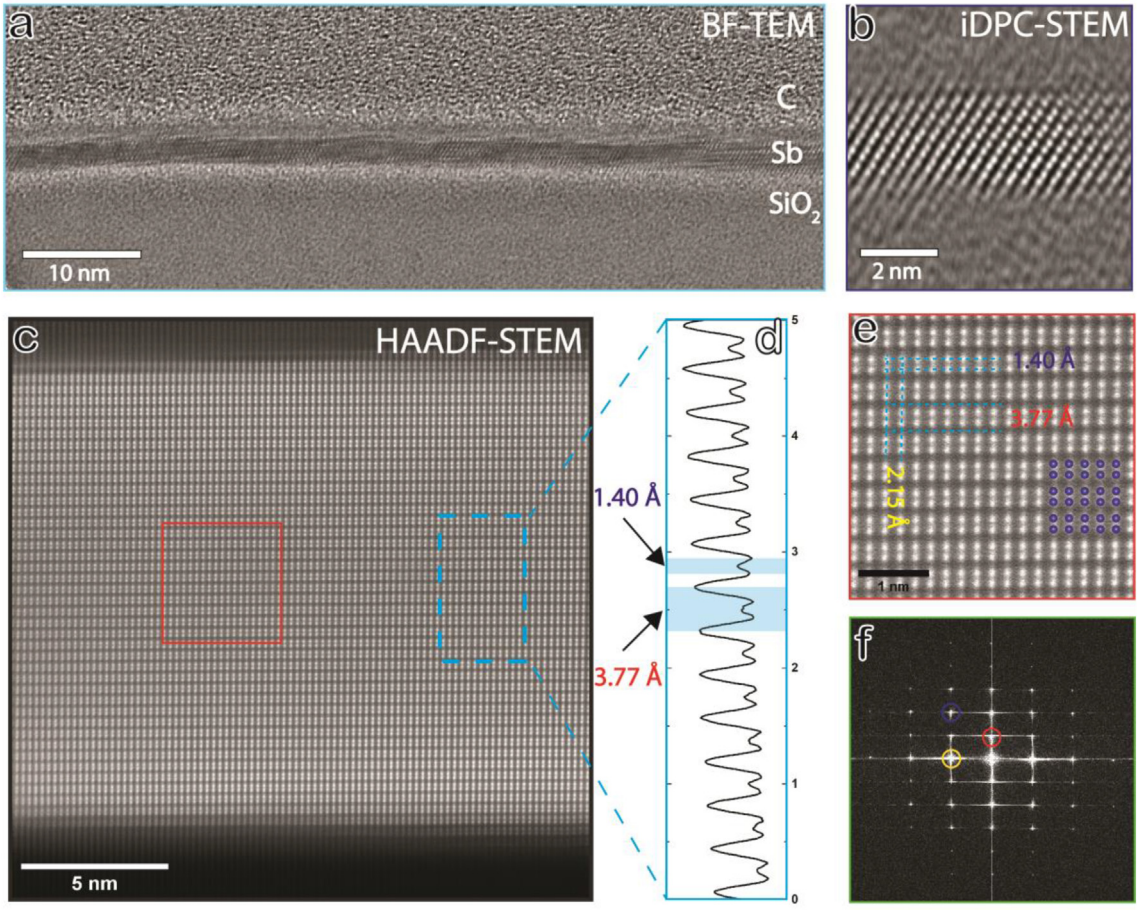


**Fig. 6.** Sb thin films were grown using PLD, and a thin seed layer technique was used such that the Sb bilayers were everywhere parallel to the $SiO_2$ substrate surface. (a) BF-TEM image of a few layers of Sb/antimonene on $SiO_2$ substrate showing full surface coverage. (b) The iDPC-STEM image of a single crystal of Sb/antimonene layers with c-axis out-of-plane orientation. (c) Overview HAADF-STEM image showing the entire thickness of about 20 nm of the Sb film. The bottom $SiO_2$ substrate and the top carbon capping layer are readily visible. (d) An intensity line profile for the indicated blue dashed region allowing quantifying interplanar distances and vdW-like gaps and (e) a magnified view of an area indicated by the red box in (c). (f) The FFT pattern was extracted from (e). FFT, fast Fourier transform; HAADF, high-angle annular dark-field; iDPC, integrated differential phase contrast; PLD, pulsed laser deposition; STEM, scanning transmission electron microscopy; BF-TEM, bright field mode transmission electron microscopy.

Supplementary Information 2. The few layers of antimonene formed on a $SiO_2$ substrate have a complete full coverage and an extremely smooth surface, suitable for use as a template. Fig. 6c shows a cross-sectional HAADF-STEM image of homoepitaxially grown Sb film on $SiO_2$ substrate. Here, the layered Sb with c-axis out-of-plane orientation (as viewed in [10 $\bar{1}$ 0] zone axis orientation) sandwiched between the bottom $SiO_2$ layer and the top carbon capping layer can be observed with clearly isolated interfaces. The crystalline Sb film has an overall thickness of about 20 nm. A magnified view of an area indicated by a red box is shown in Fig. 6e. The STEM images show a vdW-like gap separating the Sb bilayers. In Fig. 6d, an intensity line profile is plotted for the blue dashed rectangular area indicated in Fig. 6c. Blue overlay boxes in Fig. 6d distinguish the separation for Sb−Sb bilayers and the vdW-like gaps. We measured an interplanar separation distance of ≈1.40 Å between the Sb atoms within the bilayer and a distance of ≈3.77 Å for the vdW-like separation between the bilayers (i.e. the vdW gap itself is ≈2.37 Å which is close to the 2.44 Å measured above for Sb bilayers on $Sb_2Te_3$).

Our work demonstrated the possibility of producing high-quality Sb thin films using PLD. By fine-tuning the deposition parameters, the c-axis out-of-plane growth of Sb thin films was achieved on lattice matching $Sb_2Te_3$ and amorphous $SiO_2/Si_3N_4$ substrates. The quality and texture of the deposited thin films were monitored *in situ* using RHEED and ex-situ using high-resolution electron microscopy. The structural analysis of the thin films revealed the production of the most stable allotrope β-phase antimony with a trigonal crystal structure. Previously reported works, where MBE and physical vapor deposition was employed (since no reported work exists for Sb thin film production using PLD), show the difficulty of producing smooth, high-quality Sb thin films. The reported results mainly show Sb islands and flakes on crystalline substrates like graphene and sapphire [32,33,38−40,50,51]. In contrast, our Sb thin films show smooth thin films with continuous and complete substrate coverage. This can be seen from the SEM, AFM, and HAADF-STEM results presented in this work. Even more interesting is our ability to produce purely c-axis out-of-plane Sb thin films on any amorphous substrate. The thin films can also be relatively small in thickness with only few layers of Sb stacked as seen in Fig. 6a and b. Fig. S2a also shows the initial amorphous seed layer which has a thickness of about 3 nm. In addition, we previously reported our ability to produce high-quality Sb amorphous thin films with full substrate coverage and smooth surfaces. Fig. 2b and Fig. S2 from the study by Yimam and Kooi [28] clearly show the high-quality Sb thin films of relatively small thicknesses.

## 4. Conclusions

In summary, our work shows the vdW epitaxial growth of antimony thin films on a lattice-matched seed layer of $Sb_2Te_3$ and on amorphous $SiO_2$ and $Si_3N_4$ substrates using PLD. We show that extremely smooth and continuous Sb thin films with full substrate coverage can be produced by precisely controlling and fine-tuning the deposition parameters. The homo- and hetero-epitaxial growth of Sb thin films, starting from an amorphous seed layer and subsequently crystallized in a preferential trigonal structure, was confirmed to have a sharp c-axis out-of-plane texture. The texture was unveiled by RHEED and local atomic-resolution HAADF-STEM imaging. In addition, from the high-resolution atomic imaging analysis, we confirmed the formation of an intermediate phase on the Sb−$Sb_2Te_3$ tie line where the first Sb bilayer couples with the last $Sb_2Te_3$ quintuple during Sb deposition on $Sb_2Te_3$. The intermediate phase formation promoted an Sb-terminated surface, leading to a 2D growth of Sb with excellent epitaxy. Given the current interest in monatomic Sb thin films, our reported results of smooth and high-quality Sb thin films produced by PLD will stimulate further study on phase change materials and optoelectronics fields. Moreover, the ability to produce full coverage films with preferential orientation and texture control on any substrate will find new and exciting applications for monatomic Sb thin films and other layered materials.

## Credit author statement

**Daniel T Yimam:** Conceptualization, Methodology, Data curation, Formal analysis, Visualization, Software, Writing − original draft, Writing- review & editing. **Majid Ahmadi**: Data curation, Visualization, Software, Writing − review & editing. **Bart J. Kooi**: Conceptualization, Writing − review & editing, Supervision, Validation, Project administration.

## Funding

This project has received funding from the European Union's Horizon 2020 Research and Innovation Programme 'BeforeHand' (Boosting Performance of Phase Change Devices by Hetero- and Nanostructure Material Design) under Grant Agreement No. 824957.

## Declaration of competing interest

The authors declare that they have no known competing financial interests or personal relationships that could have appeared to influence the work reported in this paper.

## Data availability

Data will be made available on request.

## Acknowledgments

We thank Prof. Tamalika Banerjee, Hans de Vries, and Job van Rijn for the technical assistance of the pulsed laser deposition setup. We would also like to acknowledge support from The Zernike institute for advanced materials (ZIAM) and Groningen cognitive systems and materials center (CogniGron) to the ZIAM electron microscopy facility at the University of Groningen (RUG).

## Appendix A. Supplementary data

Supplementary data to this article can be found online at https://doi.org/10.1016/j.mtnano.2023.100365.

## References

[1] K.S. Novoselov, A.K. Geim, S.V. Morozov, D. Jiang, Y. Zhang, S.V. Dubonos, I.V. Grigorieva, A.A. Firsov, Electric field in atomically thin carbon films, Science (80-) 306 (2004) 666−669, https://doi.org/10.1126/science.1102896.
[2] C.-L. Xue, S.-C. Li, Recent progress on antimonene: from theoretical calculation to epitaxial growth, Japan. J. Appl. Phys. Prog. Rev. (2021), https://doi.org/10.35848/1347-4065/abf74e.
[3] M. Pumera, Z. Sofer, 2D monoelemental arsenene, antimonene, and bismuthene: beyond black phosphorus, Adv. Mater. 29 (2017), 1605299, https://doi.org/10.1002/adma.201605299.
[4] P. Ares, F. Aguilar-Galindo, D. Rodríguez-San-Miguel, D.A. Aldave, S. Díaz-Tendero, M. Alcamí, F. Martín, J. Gómez-Herrero, F. Zamora, Mechanical isolation of highly stable antimonene under ambient conditions, Adv. Mater. 28 (2016) 6332−6336, https://doi.org/10.1002/adma.201602128.
[5] S. Zhang, Z. Yan, Y. Li, Z. Chen, H. Zeng, S. Zhang, Z. Yan, H. Zeng, Y. Li, Z. Chen, Atomically thin arsenene and antimonene: semimetal−semiconductor and indirect−direct band-gap transitions, Angew. Chem. Int. Ed. 54 (2015) 3112−3115, https://doi.org/10.1002/ANIE.201411246.
[6] I. Hilmi, A. Lotnyk, J.W. Gerlach, P. Schumacher, B. Rauschenbach, Research update: Van-der-Waals epitaxy of layered chalcogenide Sb2Te3 thin films grown by pulsed laser deposition, Appl. Mater. 5 (2017), https://doi.org/10.1063/1.4983403.

[7] J. Momand, J.E. Boschker, R. Wang, R. Calarco, B.J. Kooi, Tailoring the epitaxy of Sb2Te3 and GeTe thin films using surface passivation, CrystEngComm 20 (2018) 340–347, https://doi.org/10.1039/c7ce01825h.
[8] M. Lanius, J. Kampmeier, C. Weyrich, S. Kölling, M. Schall, P. Schüffelgen, E. Neumann, M. Luysberg, G. Mussler, P.M. Koenraad, T. Schäpers, D. Grützmacher, P–N junctions in ultrathin topological insulator Sb2Te3/Bi2Te3 heterostructures grown by molecular beam epitaxy, Cryst. Growth Des. 16 (2016) 2057–2061, https://doi.org/10.1021/acs.cgd.5b01717.
[9] G. Zhang, H. Qin, J. Teng, J. Guo, Q. Guo, X. Dai, Z. Fang, K. Wu, Quintuple-layer epitaxy of thin films of topological insulator Bi2Se3, Appl. Phys. Lett. 95 (2009), 103702, https://doi.org/10.1063/1.3200237.
[10] N. Bansal, Y.S. Kim, E. Edrey, M. Brahlek, Y. Horibe, K. Iida, M. Tanimura, G.H. Li, T. Feng, H.D. Lee, T. Gustafsson, E. Andrei, S. Oh, Epitaxial growth of topological insulator Bi2Se3 film on Si(111) with atomically sharp interface, Thin Solid Films 520 (2011) 224–229, https://doi.org/10.1016/J.TSF.2011.07.033.
[11] A. Koma, Van der Waals epitaxy-a new epitaxial growth method for a highly lattice-mismatched system, Thin Solid Films 216 (1992) 72–76, https://doi.org/10.1016/0040-6090(92)90872-9.
[12] Y. Saito, P. Fons, A.V. Kolobov, J. Tominaga, Self-organized van der Waals epitaxy of layered chalcogenide structures, Phys. Status Solidi Basic Res. 252 (2015) 2151–2158, https://doi.org/10.1002/pssb.201552335.
[13] Y. Saito, P. Fons, L. Bolotov, N. Miyata, A.V. Kolobov, J. Tominaga, A two-step process for growth of highly oriented Sb2Te3 using sputtering, AIP Adv. 6 (2016), 45220, https://doi.org/10.1063/1.4948536.
[14] P.A. Vermeulen, J. Mulder, J. Momand, B.J. Kooi, Strain engineering of van der Waals heterostructures, Nanoscale 10 (2018) 1474–1480, https://doi.org/10.1039/c7nr07607j.
[15] H. Zhang, D.T. Yimam, S. de Graaf, J. Momand, P.A. Vermeulen, Y. Wei, B. Noheda, B.J. Kooi, Strain relaxation in "2D/2D and 2D/3D systems": highly textured mica/Bi2Te3, Sb2Te3/Bi2Te3, and Bi2Te3/GeTe heterostructures, ACS Nano 15 (2021) 2869–2879, https://doi.org/10.1021/acsnano.0c08842.
[16] I. Hilmi, A. Lotnyk, J.W. Gerlach, P. Schumacher, B. Rauschenbach, Influence of substrate dimensionality on the growth mode of epitaxial 3D-bonded GeTe thin films: from 3D to 2D growth, Mater. Des. 168 (2019), 107657, https://doi.org/10.1016/j.matdes.2019.107657.
[17] T. Lei, C. Liu, J.L. Zhao, J.M. Li, Y.P. Li, J.O. Wang, R. Wu, H.J. Qian, H.Q. Wang, K. Ibrahim, Electronic structure of antimonene grown on Sb2Te3 (111) and Bi2Te3 substrates, J. Appl. Phys. 119 (2016), 15302, https://doi.org/10.1063/1.4939281.
[18] K. Holtgrewe, S.K. Mahatha, P.M. Sheverdyaeva, P. Moras, R. Flammini, S. Colonna, F. Ronci, M. Papagno, A. Barla, L. Petaccia, Z.S. Aliev, M.B. Babanly, E.V. Chulkov, S. Sanna, C. Hogan, C. Carbone, Topologization of β-antimonene on Bi2Se3 via proximity effects, Sci. Rep. 10 (2020), https://doi.org/10.1038/s41598-020-71624-4.
[19] R. Flammini, S. Colonna, C. Hogan, S.K. Mahatha, M. Papagno, A. Barla, P.M. Sheverdyaeva, P. Moras, Z.S. Aliev, M.B. Babanly, E. V Chulkov, C. Carbone, F. Ronci, Evidence of β-antimonene at the Sb/Bi2Se3 interface, Nanotechnology 29 (2018), https://doi.org/10.1088/1361-6528/aaa2c4.
[20] C. Hogan, K. Holtgrewe, F. Ronci, S. Colonna, S. Sanna, P. Moras, P.M. Sheverdyaeva, S. Mahatha, M. Papagno, Z.S. Aliev, M. Babanly, E.V. Chulkov, C. Carbone, R. Flammini, Temperature driven phase transition at the antimonene/Bi2Se3 van der Waals heterostructure, ACS Nano 13 (2019) 10481–10489, https://doi.org/10.1021/ACSNANO.9B04377.
[21] X. Wu, Y. Shao, H. Liu, Z. Feng, Y.-L. Wang, J.-T. Sun, C. Liu, J.-O. Wang, Z.-L. Liu, S.-Y. Zhu, Y.-Q. Wang, S.-X. Du, Y.-G. Shi, K. Ibrahim, H.-J. Gao, Epitaxial growth and air-stability of monolayer antimonene on PdTe2, Adv. Mater. 29 (2017), 1605407, https://doi.org/10.1002/ADMA.201605407.
[22] S.H. Su, P.Y. Chuang, H.Y. Chen, S.C. Weng, W.C. Chen, K.D. Tsuei, C.K. Lee, S.H. Yu, M.M.C. Chou, L.W. Tu, H.T. Jeng, C.M. Tu, C.W. Luo, C.M. Cheng, T.R. Chang, J.C.A. Huang, Topological proximity-induced Dirac fermion in two-dimensional antimonene, ACS Nano 15 (2021) 15085–15095, https://doi.org/10.1021/acsnano.1c05454.
[23] M. Salinga, B. Kersting, I. Ronneberger, V.P. Jonnalagadda, X.T. Vu, M. Le Gallo, I. Giannopoulos, O. Cojocaru-Mirédin, R. Mazzarello, A. Sebastian, Monatomic phase change memory, Nat. Mater. 17 (2018) 681–685, https://doi.org/10.1038/s41563-018-0110-9.
[24] F. Jiao, B. Chen, K. Ding, K. Li, L. Wang, X. Zeng, F. Rao, Monatomic 2D phase-change memory for precise neuromorphic computing, Appl. Mater. Today 20 (2020), 100641, https://doi.org/10.1016/j.apmt.2020.100641.
[25] D. Dragoni, J. Behler, M. Bernasconi, Mechanism of amorphous phase stabilization in ultrathin films of monoatomic phase change material, Nanoscale 13 (2021) 16146–16155, https://doi.org/10.1039/d1nr03432d.
[26] Z. Cheng, T. Milne, P. Salter, J.S. Kim, S. Humphrey, M. Booth, H. Bhaskaran, Antimony thin films demonstrate programmable optical nonlinearity, Sci. Adv. 7 (2021), eabd7097, https://doi.org/10.1126/sciadv.abd7097.
[27] S. Aggarwal, T. Milne, N. Farmakidis, J. Feldmann, X. Li, Y. Shu, Z. Cheng, M. Salinga, W.H. Pernice, H. Bhaskaran, Antimony as a programmable element in integrated nanophotonics, Nano Lett. 22 (2022) 3532–3538, https://doi.org/10.1021/acs.nanolett.1c04286.
[28] D.T. Yimam, B.J. Kooi, Thickness-dependent crystallization of ultrathin antimony thin films for monatomic multilevel reflectance and phase change memory designs, ACS Appl. Mater. Interf. 14 (2022) 13593–13600, https://doi.org/10.1021/acsami.1c23974.
[29] W. Leng, Y. Chen, Q. Zhang, L. Sun, X. Shen, R. Wang, G. Wang, J.Q. Wang, T. Xu, Crystallization kinetics of monatomic antimony, Appl. Phys. Lett. 119 (2021), 171908, https://doi.org/10.1063/5.0064662.
[30] A. Debunne, K. Virwani, A. Padilla, G.W. Burr, A.J. Kellock, V.R. Deline, R.M. Shelby, B. Jackson, Evidence of crystallization–induced segregation in the phase change material Te-rich GST, J. Electrochem. Soc. 158 (2011) H965, https://doi.org/10.1149/1.3614508.
[31] D.T. Yimam, A.J.T. Van Der Ree, O. Abou El Kheir, J. Momand, M. Ahmadi, G. Palasantzas, M. Bernasconi, B.J. Kooi, Phase separation in Ge-rich GeSbTe at different length scales: melt-quenched bulk versus annealed thin films, Nanomaterials 12 (2022) 1717, https://doi.org/10.3390/NANO12101717/S1.
[32] M. Gu, C. Li, Y. Ding, K. Zhang, S. Xia, Y. Wang, M.-H. Lu, H. Lu, Y.-F. Chen, Direct growth of antimonene on C-plane sapphire by molecular beam epitaxy, Appl. Sci. 10 (2020) 639, https://doi.org/10.3390/app10020639.
[33] X. Sun, Z. Lu, Y. Xiang, Y. Wang, J. Shi, G.C. Wang, M.A. Washington, T.M. Lu, Van der Waals epitaxy of antimony islands, sheets, and thin films on single-crystalline graphene, ACS Nano 12 (2018) 6100–6108, https://doi.org/10.1021/acsnano.8b02374.
[34] Z.-Q. Shi, H. Li, Q.-Q. Yuan, C.-L. Xue, Y.-J. Xu, Y.-Y. Lv, Z.-Y. Jia, Y. Chen, W. Zhu, S.-C. Li, Kinetics-limited two-step growth of van der Waals puckered honeycomb Sb monolayer, ACS Nano 14 (2020), https://doi.org/10.1021/acsnano.0c04620.
[35] M. Fortin-Deschênes, O. Waller, T.O. Menteş, A. Locatelli, S. Mukherjee, F. Genuzio, P.L. Levesque, A. Hébert, R. Martel, O. Moutanabbir, Synthesis of antimonene on germanium, Nano Lett. 17 (2017) 4970–4975, https://doi.org/10.1021/acs.nanolett.7b02111.
[36] K. Holtgrewe, S.K. Mahatha, P.M. Sheverdyaeva, P. Moras, R. Flammini, S. Colonna, F. Ronci, M. Papagno, A. Barla, L. Petaccia, Z.S. Aliev, M.B. Babanly, E.V. Chulkov, S. Sanna, C. Hogan, C. Carbone, Topologization of β-antimonene on Bi2Se3 via proximity effects, Sci. Rep. 10 (2020), https://doi.org/10.1038/s41598-020-71624-4.
[37] C. Gibaja, D. Rodriguez-San-Miguel, P. Ares, J. Gómez-Herrero, M. Varela, R. Gillen, J. Maultzsch, F. Hauke, A. Hirsch, G. Abellán, F. Zamora, Few-layer antimonene by liquid-phase exfoliation, Angew. Chem. 128 (2016) 14557–14561, https://doi.org/10.1002/ANGE.201605298.
[38] J. Ji, X. Song, J. Liu, Z. Yan, C. Huo, S. Zhang, M. Su, L. Liao, W. Wang, Z. Ni, Y. Hao, H. Zeng, Two-dimensional antimonene single crystals grown by van der Waals epitaxy, Nat. Commun. 7 (2016), https://doi.org/10.1038/ncomms13352.
[39] R. Cecchini, C. Martella, C. Wiemer, A. Lamperti, A. Debernardi, L. Nasi, L. Lazzarini, A. Molle, M. Longo, Vapor phase epitaxy of antimonene-like nanocrystals on germanium by an MOCVD process, Appl. Surf. Sci. 535 (2021), 147729, https://doi.org/10.1016/j.apsusc.2020.147729.
[40] T. Gupta, K. Elibol, S. Hummel, M. Stöger-Pollach, C. Mangler, G. Habler, J.C. Meyer, D. Eder, B.C. Bayer, Resolving few-layer antimonene/graphene heterostructures, Npj 2D Mater. Appl. 5 (2021), https://doi.org/10.1038/s41699-021-00230-3.
[41] S. Kuriakose, S.K. Jain, S.A. Tawfik, M.J.S. Spencer, B.J. Murdoch, M. Singh, F. Rahman, E.L.H. Mayes, M.Y. Taha, R.T. Ako, V. Bansal, T. Ahmed, S. Sriram, M. Bhaskaran, S. Balendhran, S. Walia, Monocrystalline antimonene nanosheets via physical vapor deposition, Adv. Mater. Interf. 7 (2020), 2001678, https://doi.org/10.1002/admi.202001678.
[42] J.D. Yao, Z.Q. Zheng, G.W. Yang, Production of large-area 2D materials for high-performance photodetectors by pulsed-laser deposition, Prog. Mater. Sci. (2019), 100573, https://doi.org/10.1016/J.PMATSCI.2019.100573.
[43] Z. Yang, J. Hao, Progress in pulsed laser deposited two-dimensional layered materials for device applications, J. Mater. Chem. C 4 (2016) 8859, https://doi.org/10.1039/c6tc01602b.
[44] L.-P. Zhang, Y. Liu, M.K. Gautam, S. Kumar, S. Mukherjee, H. Bryja, J.W. Gerlach, A. Prager, M. Ehrhardt, B. Rauschenbach, A. Lotnyk, Epitaxial layered Sb2Te3 thin films for memory and neuromorphic applications, 2D Mater. 8 (2021), 045027, https://doi.org/10.1088/2053-1583/AC1E71.
[45] A. Lotnyk, I. Hilmi, M. Behrens, B. Rauschenbach, Temperature dependent evolution of local structure in chalcogenide-based superlattices, Appl. Surf. Sci. 536 (2021), 147959, https://doi.org/10.1016/J.APSUSC.2020.147959.
[46] S. Cecchi, D. Dragoni, D. Kriegner, E. Tisbi, E. Zallo, F. Arciprete, V. Holý, M. Bernasconi, R. Calarco, Interplay between structural and thermoelectric properties in epitaxial Sb2+xTe3 alloys, Adv. Funct. Mater. 29 (2019), 1805184. https://onlinelibrary-wiley-com.proxy-ub.rug.nl/doi/full/10.1002/adfm.201805184. (Accessed 16 August 2022).
[47] P.F.P. Poudeu, M.G. Kanatzidis, Design in solid state chemistry based on phase homologies. Sb 4Te3 and Sb8Te9 as new members of the series (Sb2Te3)m·(Sb 2)n, Chem. Commun. (2005) 2672–2674, https://doi.org/10.1039/b500695c.
[48] K. Kifune, Y. Kubota, T. Matsunaga, N. Yamada, Extremely long period-stacking structure in the Sb-Te binary system, Acta Crystallogr. Sect. B Struct. Sci. 61 (2005) 492–497, https://doi.org/10.1107/S0108768105017714.
[49] M. Nord, P.E. Vullum, I. MacLaren, T. Tybell, R. Holmestad, Atomap: a new software tool for the automated analysis of atomic resolution images using two-dimensional Gaussian fitting, Adv. Struct. Chem. Imag. 3 (2017) 9, https://doi.org/10.1186/s40679-017-0042-5.
[50] S. Xing, L. Lei, H. Dong, J. Guo, F. Cao, S. Gu, S. Hussain, F. Pang, W. Ji, R. Xu, Z. Cheng, Epitaxial growth of antimony nanofilms on HOPG and thermal desorption to control the film thickness, Chin. Phys. B 29 (2020), 96801, https://doi.org/10.1088/1674-1056/aba27c.
[51] H.A. Chen, H. Sun, C.R. Wu, Y.X. Wang, P.H. Lee, C.W. Pao, S.Y. Lin, Single-crystal antimonene films prepared by molecular beam epitaxy: selective growth and contact resistance reduction of the 2D material heterostructure, ACS Appl. Mater. Interf. 10 (2018) 15058–15064, https://doi.org/10.1021/acsami.8b02394.